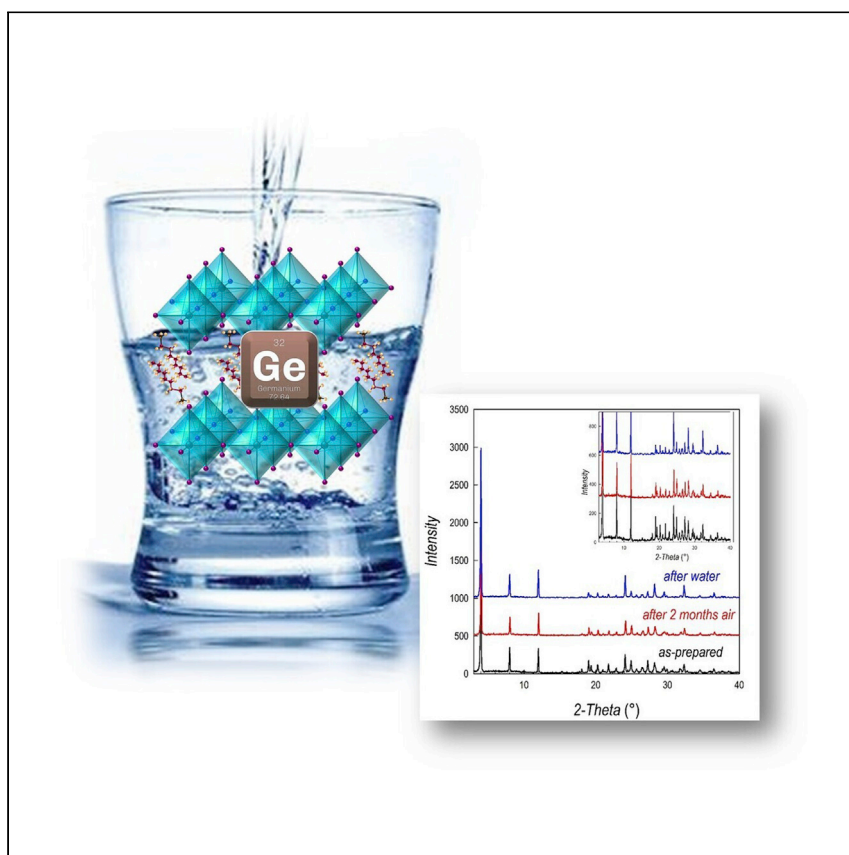


Article

Air- and water-stable and photocatalytically active germanium-based 2D perovskites by organic spacer engineering



Metal halide perovskite photocatalysis is widely studied in several applied fields. In this work, Romani et al. demonstrate 2D Ge-containing perovskite engineering to improve air and water resistance. Such characteristics are then exploited in solar-driven hydrogen generation in an aqueous environment.

Lidia Romani, Andrea Speltini, Rossella Chiara, ..., Maria Medina-Llamas, Filippo De Angelis, Lorenzo Malavasi

andrea.listorti@uniba.it (A.L.)
francesco.ambrosio@unibas.it (F.A.)
lorenzo.malavasi@unipv.it (L.M.)

Highlights

Preparation of 2D Ge-containing metal halide perovskite

Demonstration of a strategy to induce air/water resistance by cation engineering

Strategy to create heterojunctions between Ge-perovskite and carbon nitride

Demonstration of active photocatalytic activity in hydrogen generation

Article

Air- and water-stable and photocatalytically active germanium-based 2D perovskites by organic spacer engineering

Lidia Romani,^{1,2} Andrea Speltini,¹ Rossella Chiara,¹ Marta Morana,¹ Clarissa Coccia,¹ Costanza Tedesco,¹ Vincenza Armenise,³ Silvia Colella,⁴ Antonella Milella,³ Andrea Listorti,^{3,*} Antonella Profumo,¹ Francesco Ambrosio,^{5,6,7,*} Edoardo Mosconi,⁷ Riccardo Pau,^{8,9} Federico Pitzalis,⁸ Angelica Simbula,⁸ Damiano Ricciarelli,¹⁰ Michele Saba,⁸ Maria Medina-Llamas,^{1,10} Filippo De Angelis,^{7,11,12} and Lorenzo Malavasi^{1,13,*}

SUMMARY

There is increasing interest in the role of metal halide perovskites for heterogeneous catalysis. Here, we report a Ge-based 2D perovskite material that shows intrinsic water stability realized through organic cation engineering. Incorporating 4-phenylbenzylammonium (PhBz) we demonstrate, by means of extended experimental and computational results, that PhBz₂GeBr₄ and PhBz₂GeI₄ can achieve relevant air and water stability. The creation of composites embedding graphitic carbon nitride (g-C₃N₄) allows a proof of concept for light-induced hydrogen evolution in an aqueous environment by 2D Ge-based perovskites thanks to the effective charge transfer at the heterojunction between the two semiconductors.

INTRODUCTION

Metal halide perovskites (MHPs) are attracting huge interest for their possible application in heterogeneous photocatalysis following the recent synthesis of materials and heterostructures that have been found to be efficient for a plethora of photocatalyzed chemical reactions, including hydrogen generation and CO₂ reduction.^{1–17} A major limitation of MHPs in photocatalysis is their limited water stability, which derives from the high ionic character of the metal halide framework.^{2,18,19} In this context, 2D-layered MHPs may be particularly suitable to overcome this issue in virtue of the vast range of organic spacers that can be inserted as a protective barrier between the inorganic perovskite layer(s).²⁰ In fact, upon the introduction of a highly hydrophobic organic spacer in the perovskite structure, significant moisture and water stability could be achieved, and examples exist of systems forming a suspension in water instead of being dissolved.^{8,21–23} In this respect, recently, some Bi- and Sn-based perovskites with improved water resistance were found to show significant visible-light photocatalytic activity of hydrogen photogeneration and organic dye degradation, which was further enhanced by designing heterostructures with graphitic carbon nitride (g-C₃N₄).^{8,21} Similar strategies have been used also by other authors on the Cs₃Bi₂I₉ perovskite derivative.^{7,11}

While materials engineering has been successful for the synthesis of lead-free MHP photocatalysts, there are no reports about any photoactive Ge halide perovskite. Recently, a series of Ruddlesden-Popper (RP) 2D Ge bromide perovskites (n = 1), namely A₂GeBr₄, with A = C₆H₄CH₂CH₂NH₃ (phenylethylammonium [PEA]); BrC₆H₄CH₂CH₂

¹Department of Chemistry and INSTM, University of Pavia, Via Taramelli 16, 27100 Pavia, Italy

²Tecnologie di Generazione e Materiali, Ricerca sul Sistema Energetico - RSE S.p.A., Via Rubattino 54, 20134 Milano, Italy

³Department of Chemistry, University of Bari "Aldo Moro," via Orabona 4, 70126 Bari, Italy

⁴National Research Council, Institute of Nanotechnology (CNR-NANOTEC), c/o Department of Chemistry, University of Bari "Aldo Moro," via Orabona 4, 70126 Bari, Italy

⁵Dipartimento di Scienze, University of Basilicata, Viale dell'Ateneo Lucano, 10, 85100 Potenza, Italy

⁶Department of Chemistry and Biology "A. Zambelli," University of Salerno, Via Giovanni Paolo II 132, 84084 Fisciano, Salerno, Italy

⁷Computational Laboratory for Hybrid/Organic Photovoltaics (CLHYO), Istituto CNR di Scienze e Tecnologie Chimiche "Giulio Natta" (CNR-SCITEC), via Elce di Sotto 8, 06123 Perugia, Italy

⁸Department of Physics, University of Cagliari, Cittadella Universitaria S.P. Monserrato-Sestu km 0.7, 09042 Monserrato, Italy

⁹Zernike Institute for Advanced Materials, University of Groningen, Nijenborgh 4, 09747 Groningen, the Netherlands

¹⁰Unidad Académica Preparatoria, Plantel II, Universidad Autónoma de Zacatecas, Zacatecas, Zacatecas 98068, México

¹¹Department of Chemistry, Biology and Biotechnology, University of Perugia, via Elce di Sotto 8, 06123 Perugia, Italy

¹²Department of Natural Sciences & Mathematics, College of Sciences & Human Studies, Prince Mohammad Bin Fahd University, Dhahran 34754, Saudi Arabia

¹³Lead contact

*Correspondence: andrea.listorti@uniba.it (A.L.), francesco.ambrosio@unibas.it (F.A.), lorenzo.malavasi@unipv.it (L.M.)

<https://doi.org/10.1016/j.xcrp.2022.101214>



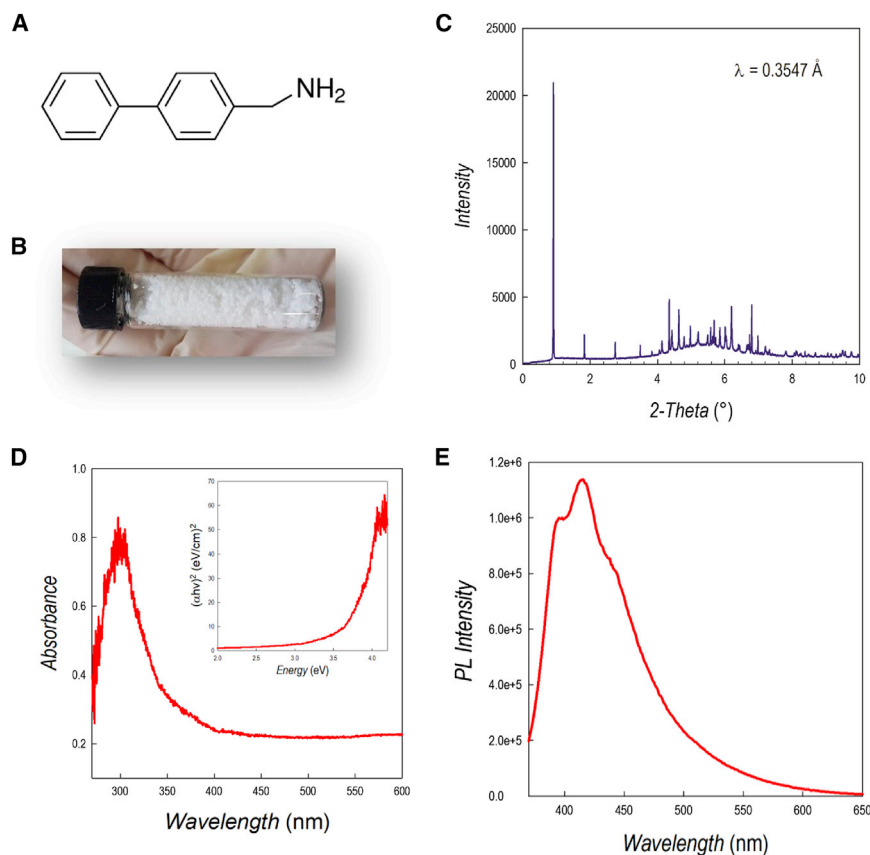


Figure 1. Structural and optical properties of PhBz₂GeBr₄

(A) Sketch of the chemical formula of 4-phenylbenzylamine.
 (B) Picture showing the appearance of the powdered sample.
 (C) SR-XRD pattern of PhBz₂GeBr₄ collected at 0.3547 Å.
 (D) Absorption spectra of PhBz₂GeBr₄ (inset: Tauc plot).
 (E) PL spectra of PhBz₂GeBr₄.

NH₃ (Br-phenylethylammonium [BrPEA]); FC₆H₄CH₂CH₂NH₃ (F-phenylethylammonium [FPEA]); and C₆H₄CH₂NH₃ (benzylammonium [BzA]), showed air stability but not water tolerance.²⁴ Therefore, we further extended this quest by designing a 2D composition including the 4-phenylbenzylammonium (PhBz) spacer cation (Figure 1A). This cation presents extended π -conjugated systems, creating a unique condition in which strong intra-layer van der Waals (vdW) interactions are established, substantially stabilizing the resulting bulk perovskite. Thanks to this stabilization, we demonstrate improved air and water stability in 2D Ge perovskites containing the PhBz cation. Such stability is exploited in the construction of heterojunctions with g-C₃N₄ and their application in the solar-driven hydrogen production in aqueous environment.

RESULTS AND DISCUSSION

PhBz₂GeBr₄ perovskite structure and stability

The novel PhBz₂GeBr₄ perovskite was synthesized by means of wet-chemistry route as described in the experimental procedures. The powder has a white color (Figure 1B), and the corresponding high-resolution synchrotron radiation (SR) powder X-ray diffraction (XRD) pattern collected at 0.3547 Å is shown in Figure 1C. The indexing of the SR-XRD data (Figure S1A) provided an orthorhombic cell (space group *Pmc2*₁) with refined lattice parameters of *a* = 6.0260(1), *b* = 9.1744(2), and

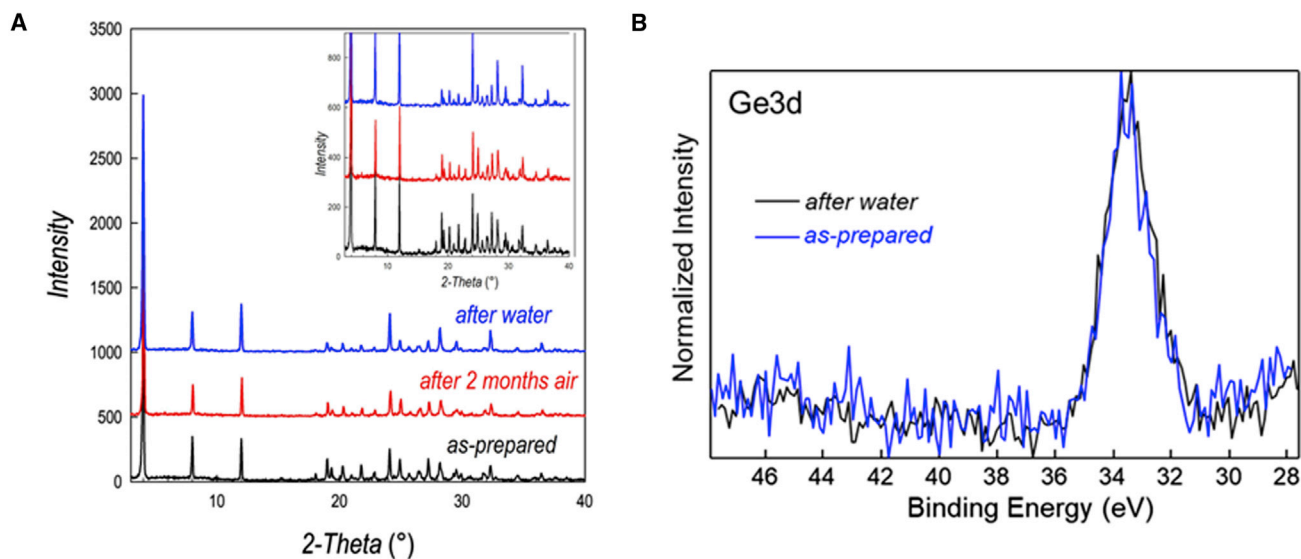


Figure 2. Air and water stability of PhBz₂GeBr₄

(A) XRD pattern of as-prepared PhBz₂GeBr₄ (black) after 2 months of air exposure (red) and after 24 h water treatment (blue). Inset: focus on a reduced 2-theta range.

(B) Ge3d XPS spectrum of as-prepared PhBz₂GeBr₄ (black) and after 24 h water treatment (blue).

$c = 44.376(1)$ Å. There are no literature reports on 2D perovskites containing PhBz cation, therefore a direct comparison with analogous compositions is not possible. The most similar material reported, in terms of organic cation, is BPEA₂PbI₄ (BPEA = 2-(4-biphenyl)ethylamine), in which the organic cation has an ethyl linked to the amine group.²⁵ Even though the central metal and the halide are different with respect to PhBz₂GeBr₄, the agreement with the symmetry of the BPEA₂PbI₄ crystal suggests a similar organic spacer arrangement as shown in Figure S1B, where PhBz₂GeBr₄ diffraction is plotted against the expected Bragg peaks from BPEA₂PbI₄. The long c axis is, as well, in a similar range as the one reported here.²⁵

The optical properties of PhBz₂GeBr₄ have been determined by UV-visible (UV-vis) absorption spectroscopy and photoluminescence (PL) (see Figures 1D and 1E). From the Tauc plot, we estimate a band gap of 3.64 eV, while the PL spectrum shows a structured intense band composed of three contributions with the main emission peak centered at about 415 nm.

To test the stability versus moisture of the synthesized material, as-prepared PhBz₂GeBr₄ (kept under argon in glovebox) was exposed to laboratory air ($T \approx 22^\circ\text{C}$, relative humidity [RH] $\approx 35\%$) for 2 months. The XRD pattern collected after this time interval shows a perfect match with the pattern of the as-prepared PhBz₂GeBr₄ (cf. red and black lines in Figure 2A). Furthermore, PhBz₂GeBr₄ powders were dispersed in water and kept under stirring for 24 h, and the diffraction pattern of the powders was found in very good agreement with the as-prepared material (cf. blue versus black patterns in Figure 2A).^{9,21} In the rescaled inset of Figure 2A, we highlighted the peaks around 10° – 40° to put in prominence the very good agreement between the patterns in the whole diffraction range.

Further evidence of water stability has been assessed through a leaching test. In this assay, PhBz₂GeBr₄ has been placed in water under magnetic stirring, and the amount of Ge in the solution has been determined by inductively coupled plasma

optical emission spectroscopy (ICP-OES) (see details in the [supplemental information](#)). After 4, 8, 16, and 24 h of stirring, the Ge amounts detected in the solution were 4.3%, 5.7%, 5.9%, and 6%, respectively, of the total amount of Ge present in the perovskites, thus confirming the high water stability and insolubility of $\text{PhBz}_2\text{GeBr}_4$.

In addition to the clear evidence of air and water structural stability reported above, we applied X-ray photoelectron spectroscopy (XPS) on the as-prepared sample and on the sample after immersion in water. The whole set of recorded spectra is shown in [Figure S2](#), while in [Figure 2B](#), we report the Ge 3d spectrum. The Ge 3d spectra of the two samples reported in [Figure 2B](#) are superimposable (as for all the other elements probed, cf. [supplemental information](#)), indicating that the Ge ions in immersed samples retain the same oxidation state of as-prepared materials.

The relative position of the Ge 3d peak suggests the possible presence of Ge(IV) on the surface of the material, possibly in the form of a native oxide, which could act as protective layer as recently proposed to justify an enhanced air stability of 2D and 3D Ge perovskites.^{26,27} More specifically, the binding energy position of the Ge 3d peaks at 33.4 eV is indicative of a Ge(IV) state and an additional indication of the Ge(IV) oxide formation at the surface of the material derives from the curve-fit analysis of the corresponding O1s spectra ([Figure S2](#)), revealing the presence of a component at 531.8 eV typical of GeO_2 .^{28,29}

However, since previously synthesized Ge-based 2D perovskites did not show any water stability, the reason of the improved water stability of $\text{PhBz}_2\text{GeBr}_4$ may predominantly lay in the bulk properties originating by the significant steric hindrance and hydrophobicity of the organic spacer.²⁴ Similar water stability has been also observed in some Sn-based MHPs, namely DMASnBr_3 and $\text{PEA}_2\text{SnBr}_4$.^{8,9} In the first material, the mechanism leading to improved stability and effective photocatalytic activity results from the valence band energy stabilization, which should reduce the exposure of the material to oxidants, restoring a value similar to MAPbI_3 , healing the material from degradation into Sn^{4+} phases and self-p-doping effects.^{30,31} On the other hand, the improved stability in $\text{PEA}_2\text{SnBr}_4$ was again related to the nature of surface-terminating groups and the presence of hydrophobic PEA moiety.⁸ For lead-based perovskites, the highly ionic nature of 3D systems has hampered their use in aqueous environments. For MAPbI_3 , for example, any photocatalytic activity has been only reported in hydrohalic acids by exploiting the dynamic equilibrium of the dissolution and precipitation of the perovskite in saturated aqueous solutions.¹⁷ More water-stable Pb-containing perovskites have been obtained by exploring the use on long aliphatic chains in 2D systems such as for $(\text{HDA})_2\text{PbI}_4$ (HAD = hexadecylammonium).²³ This phase was also used in photocatalytic activity for photoredox C–C bond cleavage and dehydrogenation catalysis but not for hydrogen photogeneration.²³

$\text{PhBz}_2\text{GeBr}_4$ hydrogen generation experiments

We exploited the advantage of $\text{PhBz}_2\text{GeBr}_4$ superior water stability by testing its possible application in photocatalysis. Hydrogen photogeneration characteristics have been determined according to a commonly employed protocol we already applied for other MHPs.^{8,9,21} First, we determined the hydrogen evolution rate (HER) of pure $\text{PhBz}_2\text{GeBr}_4$ under simulated solar light, which turned out to be $\sim 6 \mu\text{mol g}^{-1} \text{h}^{-1}$, a low but relevant value for a pure MHPs, also considering the relatively high band gap of the materials, 3.6 eV, which corresponds to efficient

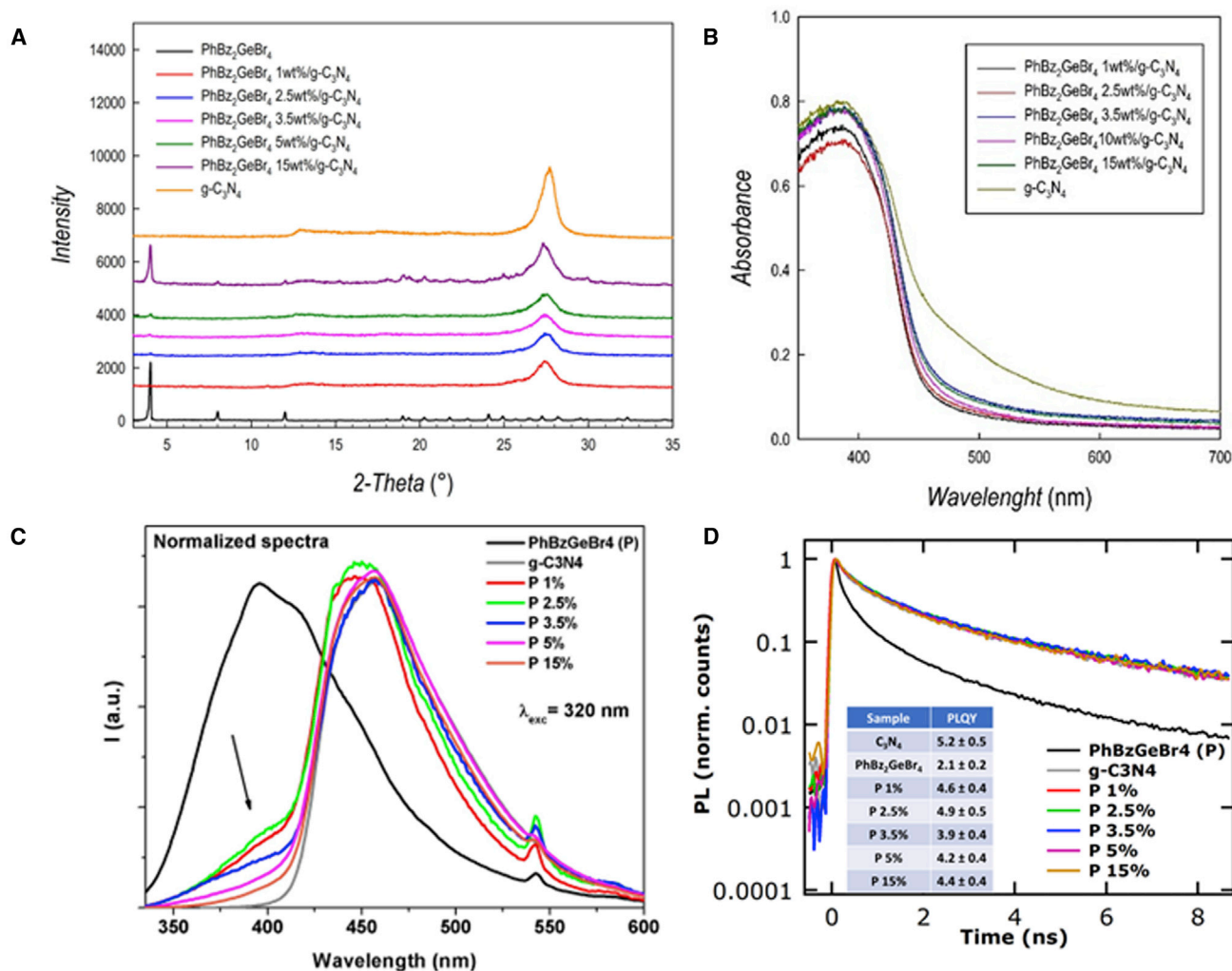


Figure 3. Structural and optical properties of PhBz₂GeBr₄/g-C₃N₄ composites

(A) XRD patterns of PhBz₂GeBr₄/g-C₃N₄ composites for different perovskite loadings.

(B) UV-vis spectra of PhBz₂GeBr₄/g-C₃N₄ composites for different perovskite loadings.

(C) Normalized emission spectra and of PhBz₂GeBr₄/g-C₃N₄ composites at different percentages of perovskite loading (wt %). g-C₃N₄ refers to pristine material. $\lambda_{exc} = 320$ nm.

(D) Normalized PL decays for the same composites ($\lambda_{exc} = 320$ nm; $\lambda_{em} = 450$ nm). In the inset, PLQY for all samples obtained with continuous wave (CW) excitation at 405nm.

absorption only in the UV region of the light spectrum (in line with the UV-vis absorption spectrum; Figure 1C). To enhance the photoactivity of the perovskite, we prepared composites with a well-known visible-light-absorbing semiconductor, namely g-C₃N₄. Composites have been synthesized by means of wet-chemistry route as reported in the experimental procedures at different weight percentages (% wt) of MHP relative to g-C₃N₄ (1%, 2.5%, 3.5%, 5%, and 15%). Morphologies of pure samples and composites have been assessed by scanning electron microscopy (SEM) and are reported in Figure S3. Figure 3A reports the XRD patterns of the composites showing the main contribution of g-C₃N₄ up to 15 wt %. We point out that the main peak of PhBz₂GeBr₄, located around 4°, is already detectable in the sample containing 2.5 wt % of perovskite. UV-vis spectra of the composites (Figure 3B) show a significant contribution to absorbance deriving from the carbon nitride.

The normalized PL spectra of pure compounds and composites are reported in [Figure 3C](#). Both pristine materials show intense luminescence bands, with $\text{PhBz}_2\text{GeBr}_4$ peaking at 415 nm and $\text{g-C}_3\text{N}_4$ at 455 nm. Their bands falling in different spectral regions allow us to monitor the contribution of the single components to the PL features of the composites. Noticeably, the composites, when excited at a wavelength that allows the absorption of both materials, show a spread PL emission overshadowed by $\text{g-C}_3\text{N}_4$ contribution. $\text{g-C}_3\text{N}_4$ emission is energetically spread spanning from 410 to 560 nm due to various deactivation paths existing within the energy band diagram of the material.³² The PL quantum yields (PLQYs) as well as the lifetimes (τ) ([Figure 3D](#)) are very similar for pristine and for $\text{g-C}_3\text{N}_4$ -containing composites. The PLQY varies from $3.9\% \pm 0.4\%$ to $5.2\% \pm 0.5\%$, and the average τ is 9.0 ± 0.5 ns for all specimens, further suggesting the central role played by carbon nitride states in the excitation deactivation path, while the PLQY of pure $\text{PhBz}_2\text{GeBr}_4$ is lower ($2.2\% \pm 0.2\%$), compatible with the shorter PL lifetime. These observations nicely fit the band structure of the junction, which is modeled below (*vide infra*). The normalized PL spectra show, however, some differences among the samples. Features of $\text{g-C}_3\text{N}_4$ dominate the spectra at high perovskite loadings, suggesting a highly efficient energy transfer from the perovskite moiety to $\text{g-C}_3\text{N}_4$. The low-loading composites show instead some minority features attributable to residual perovskite contribution ([Figure 3C](#)). For these compositions, namely 1%, 2.5%, and 3.5% loading of perovskite, the energy transfer appears somehow less effective, suggesting a possible defect-filling mechanism at the $\text{g-C}_3\text{N}_4$ /perovskite interface (see later in the text). An additional difference related to the shape of the composite emission can be found in the region of its peak (around 440–460 nm); here, the $\text{g-C}_3\text{N}_4$ and the high-loading composites show a more intense contribution at low energies, peaking their emission at 458 nm; meanwhile, low-loading composites (1% and 2.5%) show the maximum emission at 444 nm. The shape of the emission band in $\text{g-C}_3\text{N}_4$ materials can be attributed to the relative population of diverse energy transitions, withstanding a complex deactivation path for the excitation in $\text{g-C}_3\text{N}_4$ materials; in particular, the one at low energies are connected to π^* - π transition, while the one at high energies are related to deactivation of the nitrogen atom lone pair.^{32,33} In our systems, the diverse shapes suggest how differences in the relative populations of excitation/deactivation processes exist between low- and high-loading composites. The peculiar optical behavior of composites appears to be a distinctive trait of perovskite carbon nitride systems, as already described elsewhere, suggesting that low levels of perovskite doping may act on funneling the charges upon localized states.³⁴ Those active sites could be fundamental in boosting the photocatalytic performances of low-loading composites.³⁴ Such effect faded with increased perovskite loadings.

Finally, we investigated the solar-driven catalytic efficiency of the prepared composites in terms of the HER. The measurements have been carried out by employing current protocols applied in the literature for $\text{g-C}_3\text{N}_4$ -based composites, *i.e.*, in 10% (v/v) aqueous triethanolamine (TEOA), as a typical sacrificial agent and with Pt (3 wt %) as metal co-catalyst.³⁵ [Figure 4A](#) shows the HER as a function of perovskite loading, while [Figure 4B](#) shows the kinetics of the hydrogen evolution for the best-performing composite from [Figure 4A](#), namely 2.5 wt % $\text{PhBz}_2\text{GeBr}_4/\text{g-C}_3\text{N}_4$.

Noticeably, the composites display a synergic effect, providing a significant improvement of the HER of about 8 times with respect to pure carbon nitride ($81 \mu\text{mol g}^{-1} \text{h}^{-1}$) and of about 100 times with respect to pure $\text{PhBz}_2\text{GeBr}_4$ ($6 \mu\text{mol g}^{-1} \text{h}^{-1}$). The maximum HER is found at a relatively low MHP loading of 2.5 wt %, while higher perovskite percentages are not beneficial to improve the photoreaction. For the optimal

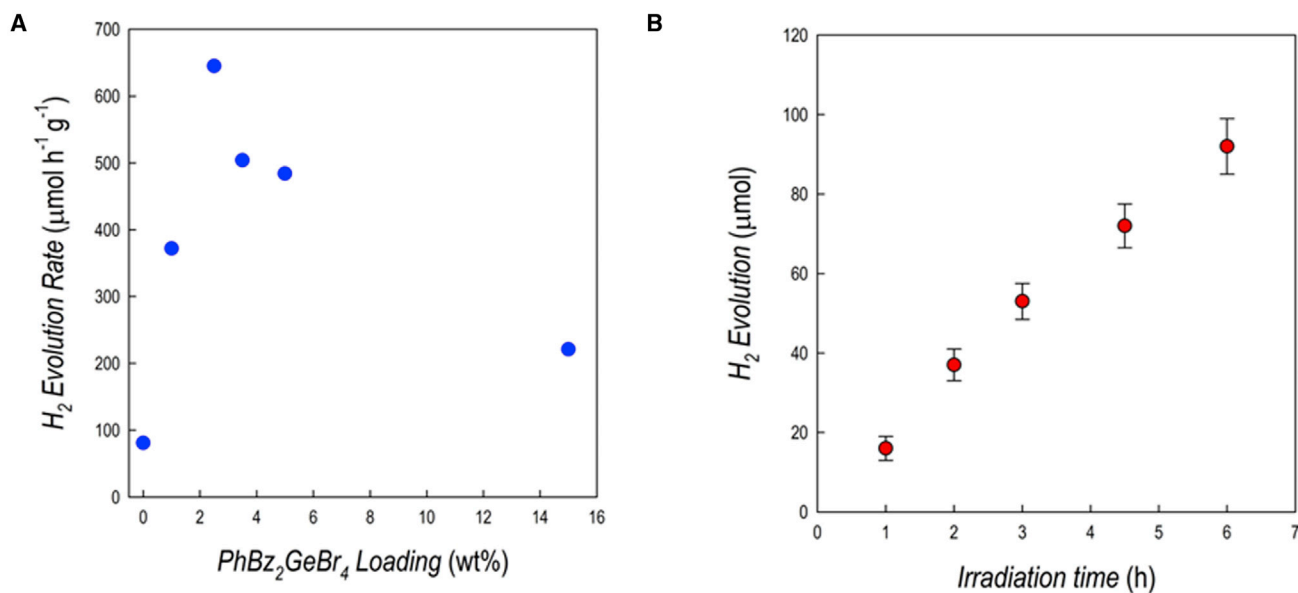


Figure 4. Hydrogen photogeneration performance of PhBz₂GeBr₄/g-C₃N₄ composites

(A) Hydrogen evolution rates for PhBz₂GeBr₄/g-C₃N₄ composites at different percentages of MHP loading, 6 h irradiation, relative standard deviation (RSD) <10% (n = 3).

(B) Hydrogen evolution profile over irradiation time for the 2.5 wt % PhBz₂GeBr₄/g-C₃N₄ composite, RSD <10% (n = 3). Conditions: 1 g L⁻¹ catalyst, 10% v/v TEOA, 3 wt % Pt, simulated solar light (Xenon lamp, 500 W m⁻², 300–800 nm, IR-treated soda-lime glass UV outdoor filter).

composite, namely at 2.5 wt %, the kinetics of H₂ evolution, reported in Figure 4B, indicates a substantial linear increase of the hydrogen production as a function of time. The value of apparent quantum yield (AQY%), calculated as the percent ratio H₂ moles/incident photons moles, for this composition (2.5 wt % of perovskite) was 5.2%.³⁶ This is the first evidence of the application of a Ge-based perovskite in solar-driven hydrogen generation; therefore, any comparison with pre-existing literature is not possible. However, the measured rates are similar to those measured for Sn- and Bi-based perovskites.^{8,9,34} The composite at 2.5 wt % of PhBz₂GeBr₄ has been tested over four successive catalytic cycles by centrifugating, recovering, and subjecting the sample to the same photocatalytic procedure. The HER in the second cycle was about 94% of the initial HER, while in both the third and fourth cycles, it was reduced to about 74% (Figure S4); such a result could be related to the slight, but detectable, Ge leaching reported above. Finally, the catalyst was recovered after a photogeneration test and analyzed by XRD to test the material stability. For the sake of clarity this test was accomplished on the material with 15 wt % loading of PhBz₂GeBr₄ since it showed the most evident reflections from the perovskite. The patterns of fresh PhBz₂GeBr₄ 15 wt %/g-C₃N₄ and of the same sample recovered after 6 h of irradiation under the conditions reported above are shown in Figure S5, indicating a very good stability of the composite after the photocatalytic test. To get a further insight into the microscopic mechanism underlying the HER behavior, we performed transient absorption spectroscopy (TAS) measurements on the composites.

Differential transmission (DT/T) measurements were performed on thin films of different PhBz₂GeBr₄/g-C₃N₄ composites on quartz substrate, which we exploit to probe carrier dynamics. Note that, oftentimes, the technique is referred to as TAS since DT/T and absorption are linked and can be converted into each other. DT/T allows us to detect the changes in optical absorption that are induced by ultrafast laser pulses, in our case constituted by 100 fs-long pulses that are 320 nm in

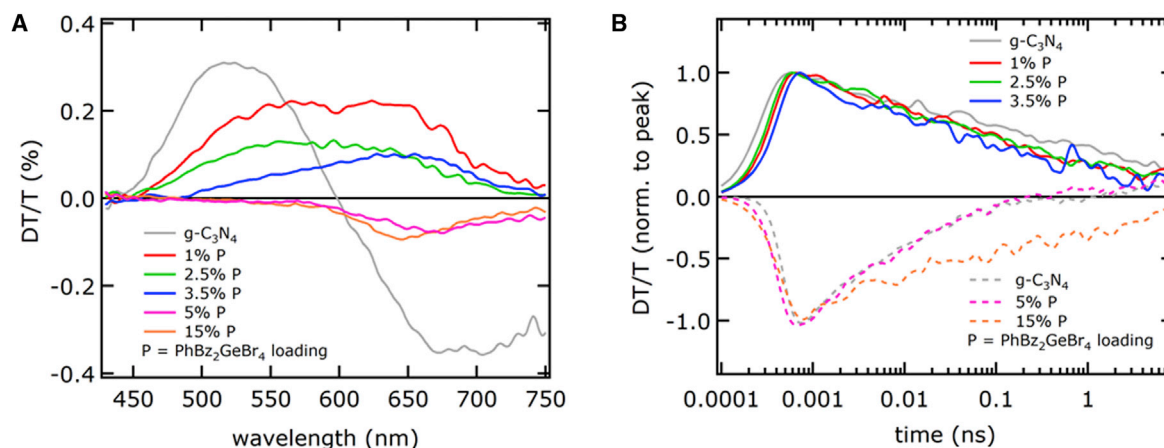


Figure 5. Transient absorption spectroscopy study of PhBz₂GeBr₄/g-C₃N₄ composites

Results of differential transmission on thin films of g-C₃N₄ with different PhBz₂GeBr₄ loadings, with excitation wavelength 320 nm.

(A) Differential transmission spectra integrated over time.

(B) Time decays of differential transmission signals integrated over wavelength, normalized for clear comparison, with bleaching features (positive) represented as solid lines, and negative bands (photoinduced absorption) depicted as dashed lines.

wavelength. DT/T is then determined with a pump-and-probe technique where fs supercontinuum white pulses are delayed with respect to pump pulses with an adjustable delay line (see the experimental section in the [supplemental information](#)). From the results collected in [Figure 5](#), two broad DT/T features are visible in g-C₃N₄ sample (gray line): a positive bleaching band around 500 nm, resulting from filling of the excited state, and a negative band, which peaked around 650 nm, that can be associated with photoinduced absorption from the excited state. When adding PhBz₂GeBr₄ from 1 to 3.5 wt %, the 500 nm-bleaching band is gradually replaced by a lower-energy one centered around 650 nm. In contrast, for % wt >5, a photoinduced band, similar to pure g-C₃N₄, is partially recovered.

The simultaneous fading of photoinduced signal/high-energy bleaching and the appearance of low-energy bleaching in DT/T spectra may be interpreted as evidence for defect filling at the g-C₃N₄/perovskite interface, possibly due to charge transfer. Both PL band structure and bleaching in DT/T can be therefore correlated with partial charge transfer to g-C₃N₄, which happens to be more efficient for intermediate compositions (1%–3.5% loading), leading to better photocatalytic performance. At variance with this, samples with above 5 wt % have PL and DT/T spectra more similar to g-C₃N₄, an indication that most photoexcited electrons are kept in g-C₃N₄ states, leading to either radiative recombination or to photoinduced absorption. Such a trend with respect to perovskite loading is compatible with what has been already observed in a Bi-based perovskite composite for photocatalysis.³⁴ The trend of both a DT/T bleaching feature and hydrogen production rate can be linked with defect filling at the g-C₃N₄/perovskite interfaces but with a disclaimer: the defect states involved in absorption process, affecting DT/T dynamics, are substantially not taking part in PL emission, which results instead from g-C₃N₄ states. In fact, the results of time-resolved PL measurements show that the PL lifetime of g-C₃N₄/perovskite compounds is not different from that of g-C₃N₄ and is not varying with perovskite loading, despite pure perovskite showing a much shorter lifetime than g-C₃N₄ compounds (see [Figure 3D](#)).

Computational modeling

The origin of the reported results was further investigated from an atomistic perspective with the aim of understanding (1) the outstanding water stability of

Table 1. Calculated values of $E_f(\text{bulk})$ and $E_f(V_A)$ (cf. main text for definitions) for the considered $A_2\text{GeX}_4$ perovskites

Perovskite	$E_f(\text{bulk})$	$E_f(V_A)$	Water stable?
$\text{PEA}_2\text{GeBr}_4$	-4.15	3.98	no
$\text{BrPEA}_2\text{GeBr}_4$	-4.12	4.18	no
$(\text{BPEA})_2\text{GeI}_4$	-4.65	4.92	yes
$(\text{BPEA})_2\text{GeBr}_4$	-4.80	5.26	yes

the Ge-based perovskites synthesized in this work, and (2) the efficient photocatalytic production of H_2 when the perovskites are used in a composite with $g\text{-C}_3\text{N}_4$ (see [Note S1](#)). In addition, computational modeling was extended to also include the iodide-analogous phase, namely $\text{PhBz}_2\text{GeI}_4$, to determine its possible application in photocatalysis. As a matter of fact, the presence of iodide can red shift the band gap and provide a more effective charge transfer in the heterostructure.^{20,24,26} However, iodide-based materials are known to be less stable than the bromide counterparts.

To fulfill the first goal, we calculated the bulk formation energies $E_f(\text{bulk})$ of the water-stable Ge-based perovskites, and we compared them with those of previously synthesized materials, bearing different A-site spacer cations, which were found to dissolve in aqueous environment.²⁴ Since no experimental crystallographic structure is currently available for $\text{PhBz}_2\text{GeI}_4$ and $\text{PhBz}_2\text{GeBr}_4$, we consider the perovskites with BPEA, which differs from PhBz only for an extra CH_2 between the aromatic ring and the ammonium moiety.²⁵ $\text{BPEA}_2\text{GeI}_4$ and $\text{BPEA}_2\text{GeBr}_4$ were modeled starting from the analogous $\text{BPEA}_2\text{PbI}_4$ as described in the [supplemental information](#). We consider, for our comparison, PEA_2GeI_4 and $\text{BrPEA}_2\text{GeBr}_4$, which have been synthesized and characterized in Chiara et al.²⁴ The details of the structural models are reported in the [supplemental information](#).

From the following reaction



where $A = \text{PEA}, \text{BrPEA}, \text{and BPEA}$ and $X = \text{Br and I}$, we define $E_f(\text{bulk})$ as follows:

$$E_f(\text{bulk}) = E(A_2\text{GeX}_4) - E(AX) - E(\text{GeX}_2). \quad (\text{Equation 2})$$

In [Equation 2](#), $E(A_2\text{GeX}_4)$, $E(AX)$, and $E(\text{GeX}_2)$ are the total energies of $A_2\text{GeX}_4$, AX , and GeX_2 , which are calculated from their respective atomistic models (cf. [Note S1](#)). Results collected in [Table 1](#) clearly indicate that perovskites bearing BPEA as spacer A-site cation are substantially more stable than the others, with formation energies being up to 0.7 eV lower. Such a larger stability may be ascribed to the enhanced vdW interactions available within the A-cation layers separating the inorganic frameworks when using the larger BPEA molecule. In order to further verify this consideration, we calculate for each studied material the formation energy of a neutral A vacancy, V_A , which is defined as

$$E_f(V_A) = E(V_A) - E(A_2\text{GeX}_4) - E(A), \quad (\text{Equation 3})$$

where $E(V_A)$ is the total energy of the perovskite model with a missing A molecule and $E(A)$ the total energy of an isolated A molecule. From [Table 1](#), we evince that the energy associated with the removal of an A cation from the bulk perovskite is remarkably higher (up to 1 eV) for BPEA when compared with the other systems, thus clearly indicating that intra-layer vdW interactions sizably stabilize BPEA perovskites. Furthermore, the higher solvation Gibbs free energies calculated for BPEA and PhBz (cf. [Table S4](#)) indicate a reduced tendency of these cations to dissolve in water when

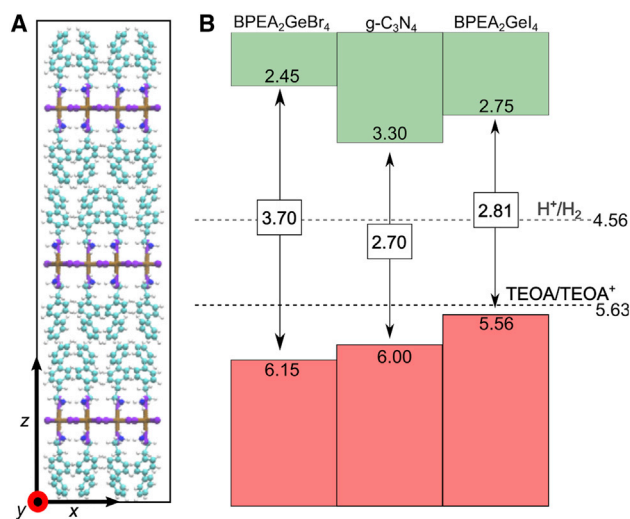


Figure 6. Computational modeling of surface termination and band alignment for BPEA₂GeI₄ and BPEA₂GeBr₄

(A) Stick-and-ball representation of the atomistic model for the (BPEA)I-terminated (100) slab of BPEA₂GeI₄ perovskite. Ge atoms are depicted in ochre, I in violet, C in cyan, N in blue, and H in white.

(B) Valence band (VB) and conduction band (CB) edges of g-C₃N₄, BPEA₂GeI₄, and BPEA₂GeBr₄ referred to the vacuum level. The energy level of standard hydrogen electrode calculated in Romani et al.⁹ and the TEOA/TEOA⁺ redox level are reported as dashed lines.

compared with the cations employed in previous work.²⁴ We note that such a result is in line with a previous observation of the increased water stability observed when replacing methylammonium with dimethylammonium in tin perovskites.^{31,37}

To study the beneficial effect on the photocatalytic H₂ production of the (BPEA)₂GeX₄ perovskites in a composite with g-C₃N₄, we investigated their band alignment. To this end, we constructed atomistic models of the surface of these materials. When considering the (100) surface of (BPEA)₂GeX₄, we find that the most stable termination is the stoichiometric (BPEA)X-terminated one, with the BPEA cations pointing their hydrophobic biphenyl moieties toward the surface (cf. Figure 6A for the (BPEA)I-terminated surface of (BPEA)₂GeI₄), while the ammonium moieties interact with the subsurface inorganic chain. This termination features a surface energy as small as 0.005 eV/Å² (cf. supplemental information for details of the calculations).

Then, we employed advanced electronic-structure calculations to evaluate the band gap of the materials and align the band edges with respect to the vacuum level (cf. Note S1 and Tables S2 and S3). The band alignment for (BPEA)₂GeI₄ and (BPEA)₂GeBr₄ is reported in Figure 6B along with that previously calculated in Romani et al.⁹ for g-C₃N₄. The band edges of (BPEA)₂GeI₄ are found to be favorably aligned with respect to those of g-C₃N₄, thus promoting the transfer of photogenerated charges in a type II heterojunction, which could also improve the carrier lifetime. At variance with this, (BPEA)₂GeBr₄, which features a larger band gap (3.7 versus 2.81 eV), has a valence band edge at an energy 0.15 eV lower than g-C₃N₄, providing a type I heterojunction. This implies that hole transfer from g-C₃N₄ to the perovskites might be subject to a small energy barrier, which may reduce the efficiency of the composite.

The results of the computational modeling have put in prominence two main results: (1) confirmation of the water stability for BPEA₂GeBr₄ together with a beneficial band

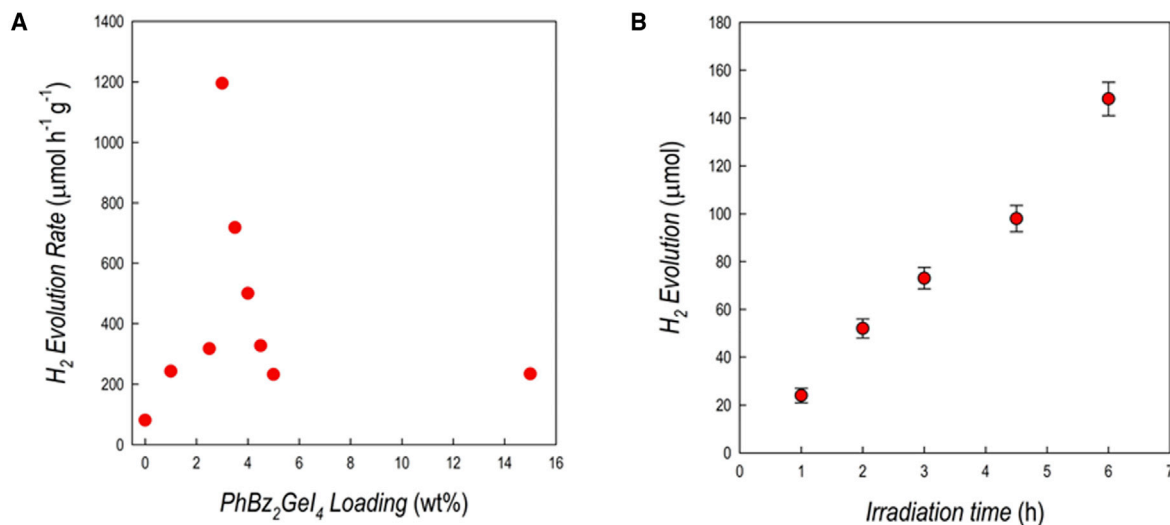


Figure 7. Hydrogen photogeneration performance of PhBz₂GeI₄/g-C₃N₄ composites

(A) Hydrogen evolution rates for PhBz₂GeI₄/g-C₃N₄ composites, 6 h irradiation, RSD <15% (n = 3).

(B) Hydrogen evolution profile over irradiation time for the 3 wt % PhBz₂GeI₄/g-C₃N₄ composite, RSD <10% (n = 3). Conditions: 1 g L⁻¹ catalyst, 10% v/v TEOA, 3 wt % Pt, simulated solar light (Xenon lamp, 500 W m⁻², 300–800 nm, IR-treated soda-lime glass UV outdoor filter).

alignment with g-C₃N₄, as demonstrated by the above reported hydrogen photogeneration experiments, and (2) prediction of good water stability by BPEA₂GeI₄ (even though it has lower E_f(bulk) and E_f(V_A) with respect to BPEA₂GeBr₄) and possible superior photocatalytic performance due to a better band alignment with respect to the bromide-containing counterpart.

PhBz₂GeI₄ hydrogen generation experiments

To test this last computational evidence, we synthesized the PhBz₂GeI₄ perovskite and a series of composites with g-C₃N₄ (1%, 2.5%, 3%, 3.5%, 4%, 4.5%, 5%, and 15% of perovskite loading). Figures S6 and S7 report the XRD and absorbance data on the composite. We used the same approach we employed for PhBz₂GeBr₄ in testing the air and water stability of PhBz₂GeI₄. Figure S8 also shows good air and water stabilities for the iodide-containing perovskites according to the computational prediction. However, the leaching test revealed an amount of Ge in the solution of about 40% already after 4 h of stirring. This value remains constant after 8 and 16 h of stirring (42% and 43%), suggesting the possible occurrence of a solubility equilibrium that then keeps the perovskite unchanged in the solution according to the XRD diffraction after recovering the powder (Figure S8). Substantially the same leaching (44%) was noticed also under photocatalytic conditions, turning in line with the overall good photocatalytic performance of this composite, described hereafter. Even though the PhBz₂GeI₄ is less stable in water, which also agrees with the calculated values of E_f(bulk), E_f(V_A), we performed a thorough investigation of the hydrogen photogeneration efficiency. Figure 7A reports the HER as a function of perovskite loading for the PhBz₂GeI₄/g-C₃N₄ composites, while Figure 7B shows the kinetics of the hydrogen photogeneration for the best-performing composite from Figure 7A, namely 3 wt % PhBz₂GeI₄/g-C₃N₄. For this system, the AQY% is 2.8%, which is lower with respect to the best-performing PhBz₂GeBr₄/g-C₃N₄ composite. The higher HER with a lower AQY (calculated as the percent ratio H₂ moles/incident photons moles) is in line with the presence of iodide extending the absorption in the visible part of the spectrum, allowing it to harness more photons. The overall result for the HER of PhBz₂

GeBr₄/g-C₃N₄ composites is observed to be higher, but the AQY is not, for a diverse absorptivity of the specimens.

The HER for the PhBz₂GeI₄/g-C₃N₄ composites is higher with respect to the PhBz₂GeBr₄/g-C₃N₄ composites, reaching a value of about 1,200 μmol g⁻¹ h⁻¹, again with a synergic effect with respect to pure carbon nitride (81 μmol g⁻¹ h⁻¹), and of about 600 times with respect to pure PhBz₂GeI₄ (2 μmol g⁻¹ h⁻¹). The maximum HER is found at 3 wt %, very close to the value of 2.5 wt % found for the PhBz₂GeBr₄/g-C₃N₄ series. Again, according to the computational modeling, we could confirm the better band alignment of this perovskite with g-C₃N₄, leading to a better performing heterostructure. While this composite proved to be less stable than the bromide counterpart, these results pave the way to further explore this system by improving its stability in water through encapsulations strategies. It is also interesting to confirm the trend as a function of loading, which peaks around 3%, in agreement with the TAS results reported above and with the previous results we provided on the Cs₃Bi₂Br₉/g-C₃N₄ composites.³⁴

Finally, to evaluate the potential of the two best-performing composites for practical photocatalytic applications, 2.5 wt % PhBz₂GeBr₄/g-C₃N₄ and 3 wt % PhBz₂GeI₄/g-C₃N₄ were tested for H₂ evolution from aqueous solutions of glucose and starch, chosen as representative biomass derivatives. Under optimized conditions, H₂ formation was appreciable for both catalysts (Table S1) and was still higher using the iodine-based composite and with a greater H₂ yield in the presence of the monosaccharide, which exhibits faster mass transfer kinetics compared with the branched-skeleton polysaccharide.³⁶ The observed HERs are clearly higher than those of the control samples (no catalysts, <0.008 μmol h⁻¹), demonstrating the effectiveness of such new composites for H₂ photogeneration also from biomasses in solution.

In conclusion, we report on the realization of an intrinsically water stable 2D Ge-based halide perovskite, a material that can sustain suspension in water for several hours. The strategy employed for the realization of such innovative system foresees the use of an extended π-conjugated organic cation (phenylbenzylammonium), which, through intra-layer vdW interactions, sizably stabilizes the resulting bulk perovskite. The material has been tested therefore for simulated solar-light-induced hydrogen evolution from water and aqueous solutions of glucose and starch in combination with a partnering material, which induces the formation of an active heterojunction, leading to very promising HERs up to 1,200 μmol g⁻¹ h⁻¹. This is an outstanding result considering the seminal exploitation of a Ge perovskite for such a purpose and provide a proof of concept for the use of 2D Ge-based MHPs. Most importantly, these findings contribute to expand the rationale behind the intelligent design of intrinsically water-stable MHP phases. The achievement of such an understating would massively impact MHP-based photocatalytic applications but also alternative optoelectronic innovations based on classes of materials such as LED, photovoltaics (PV), and detectors, whose technological declination has been delayed, among other factors, by moisture-exposure weakness of the active material.

EXPERIMENTAL PROCEDURES

Resource availability

Lead contact

Further information and requests for resources and reagents should be directed to and will be fulfilled by the lead contact, Lorenzo Malavasi (lorenzo.malavasi@unipv.it), and the other corresponding authors (andrea.listorti@uniba.it and francesco.ambrosio@unibas.it).

Materials availability

All unique or stable reagents generated in this study are available from the [lead contact](#) with a completed materials transfer agreement.

Data and code availability

The authors declare that the data supporting the findings of this study are available within the article and the [supplemental information](#).

Sample preparation

Bulk $g\text{-C}_3\text{N}_4$ has been synthesized from the polymerization of DCD ($\text{NH}_2\text{C(=NH)NHCN}$, Aldrich, 99%) by the following thermal treatment (under N_2 flux): heating ($1^\circ\text{C}/\text{min}$) to 550°C , isothermal step for 4 h followed by cooling to room temperature ($10^\circ\text{C}/\text{min}$). Synthesis has been carried out in a partially closed alumina crucible. $\text{PhBz}_2\text{GeX}_4$ ($X = \text{I}$ and Br) perovskites have been prepared by dissolving GeO_2 in HX under stirring and under nitrogen flux. The $\text{PhBz}_2\text{GeX}_4/g\text{-C}_3\text{N}_4$ composites have been prepared by adding to the DMF solution containing the perovskites the proper amount of $g\text{-C}_3\text{N}_4$ prepared as described above.

Sample characterization

The crystal structure of the samples has been characterized by room-temperature Cu-radiation XRD acquired with a Bruker D8 diffractometer. Diffuse reflectance spectroscopy (DRS) spectra were acquired in the wavelength range 300–800 nm directly on the powders by using a Jasco V-750 spectrophotometer, equipped with an integrating sphere (Jasco ISV-922). Microstructural characterization of the samples was made using a high-resolution SEM (TESCAN Mira 3) operated at 25 kV. Elemental mapping has been performed on the best-performing and stable composite (cf. section “ $\text{PhBz}_2\text{GeBr}_4$ hydrogen generation experiments”), namely 2.5 wt % $\text{PhBz}_2\text{GeBr}_4/g\text{-C}_3\text{N}_4$, and the data are reported in [Figure S9](#). Due to the very low amount of metal present in the sample, clear distribution has been obtained only for the Br, C, and N elements, indicating a good distribution of the perovskite in the carbon nitride matrix.

The PL measurements were recorded by means of a Fluorolog-3 spectrofluorometer (HORIBA Jobin-Yvon) equipped with a 450 W xenon lamp as the exciting source and double grating excitation and emission monochromators. All optical measurements were performed at room temperature on powder dispersed samples as obtained from the synthesis without any size sorting treatment. The PL emission spectra were recorded by using an excitation wavelength of 375 nm.

The DT/T was measured on the composites dispersed in Nafion matrix by exciting them with a pulsed laser source (100 fs pulses at 320 nm wavelength) obtained from a kHz regenerative amplifier and an optical parametric oscillator (Coherent Libra and Light Conversion Topas 800). DT/T is then determined with a pump-and-probe technique, where the sample is excited also with fs supercontinuum white pulses, obtained by focusing the fundamental output regenerative amplifier (800 nm) onto a sapphire plate, whose delay with respect to pump pulses is controlled with an adjustable mechanical delay line. DT/T spectra are finally obtained from signal and reference spectra acquired with a couple of CMOS grating spectrometers (Ultrafast Systems Helios).

Hydrogen evolution experiments

H_2 evolution experiments were conducted in distilled water containing 10% (v/v) TEAO (Aldrich, $\geq 99\%$), irradiated in Pyrex glass containers (28 mL capacity, 21 mL

sample). After the addition of the catalyst (1 g L^{-1}), the sample was deoxygenated by Ar bubbling (20 min) to obtain anoxic conditions and irradiated under magnetic stirring for 6 h.

Chloroplatinic acid (H_2PtCl_6 , 38% Pt basis), used as precursor for metallic Pt, was from Sigma-Aldrich. Since Pt is *in situ* photodeposited on the catalyst surface, after Ar bubbling, a small volume from a $15 \text{ g L}^{-1} \text{ H}_2\text{PtCl}_6$ aqueous solution was added, using a 10–100 μL micropipette, to the catalyst suspension (1 g L^{-1}) directly in the photoreactor. The latter was closed with sleeve stopper septa and was irradiated, as described in the following, achieving simultaneous Pt deposition and H_2 production. Irradiation was performed under simulated solar light (1,500 W Xenon lamp, 300–800 nm) using a Solar Box 1500e (CO.FO.ME.GRA S.r.l., Milan, Italy) set at a power factor 500 W m^{-2} and equipped with UV outdoor filter made of infrared (IR)-treated soda-lime glass. Triplicate photoproduction experiments were performed on all samples. The headspace-evolved gas was quantified by gas chromatography coupled with thermal conductivity detection (GC-TCD). The results obtained in terms of H_2 evolution rate are expressed in the paper as $\mu\text{moles of gas per gram of catalyst per hour}$ ($\mu\text{moles g}^{-1} \text{ h}^{-1}$). XRD measurements on spent catalysts have been done by filtering the suspensions and recovering the powder, which underwent diffraction measurements.

Metal leaching tests

The leaching tests were performed by dispersion of the powders in distilled water under magnetic stirring for 4, 8, 16, and 24 h. Then, the suspension was filtered on 0.2 μm nylon membrane, and the amount of tin in solution was determined by ICP-OES analysis after acidification (1% v/v ultrapure nitric acid).

SUPPLEMENTAL INFORMATION

Supplemental information can be found online at <https://doi.org/10.1016/j.xcrp.2022.101214>.

ACKNOWLEDGMENTS

F.A., E.M., and F.D.A. acknowledge support from the Ministero Istruzione dell'Università e della Ricerca (MIUR) and the University of Perugia through the program "Dipartimenti di Eccellenza 2018–2022" (grant AMIS) and from the European Union's Horizon 2020 research and innovation program under grant agreement no. 764047 of the Espresso project. This work has been financed by the Research Fund for the Italian Electrical System under the contract agreement between RSE S.p.A. and the Ministry of Economic Development - General Directorate for the Electricity Market, Renewable Energy and Energy Efficiency, Nuclear Energy, in compliance with the Decree of April 16th, 2018. A.S. was supported by PON "Ricerca e Innovazione" 2014–2020 FSE, project AIM1809115-2. A.L. acknowledges support from Puglia regional council (grant name: Perseo, CUP: H95F20000890003).

AUTHOR CONTRIBUTIONS

L.R., M.M.-L., C.C., and C.T. performed photocatalysis experiments; A.S. and A.P. supervised photocatalysis experiments and analyzed the data; M.M. carried out structural characterization; V.A., S.C., A.M., and A.L. performed part of the optical characterization and XPS experiments; F.A., E.M., D.R., and F.D.A. performed computational modeling work and analyzed the data, R.P., F.P., A.S., and M.S. carried out TAS measurements and related data analysis; and L.M. devised the work.

The manuscript was written by L.M., A.L., and F.A. All authors have approved the final version of the manuscript.

DECLARATION OF INTERESTS

The authors declare no competing interests.

Received: April 29, 2022

Revised: November 22, 2022

Accepted: December 8, 2022

Published: January 5, 2023

REFERENCES

- Romani, L., and Malavasi, L. (2020). Solar-driven hydrogen generation by metal halide perovskites: materials, approaches, and mechanistic view. *ACS Omega* 5, 25511–25519. <https://doi.org/10.1021/acsomega.0c03829>.
- Huang, H., Pradhan, B., Hofkens, J., Roeffaers, M.B.J., and Steele, J.A. (2020). Solar-driven metal halide perovskite photocatalysis: design, stability, and performance. *ACS Energy Lett.* 5, 1107–1123. <https://doi.org/10.1021/acsenergylett.0c00058>.
- Bresolin, B.-M., Park, Y., and Bahnemann, D. (2020). Recent progresses on metal halide perovskite-based material as potential photocatalyst. *Catalysts* 10, 709. <https://doi.org/10.3390/catal10060709>.
- Huynh, K.A., Nguyen, D.L.T., Nguyen, V., Vo, D.N., Trinh, Q.T., Nguyen, T.P., Kim, S.Y., and Le, Q.V. (2020). Halide perovskite photocatalysis: progress and perspectives. *J. Chem. Technol. Biotechnol.* 95, 2579–2596. <https://doi.org/10.1002/jctb.6342>.
- Armenise, V., Colella, S., Fracassi, F., and Listorti, A. (2021). Lead-free metal halide perovskites for hydrogen evolution from aqueous solutions. *Nanomaterials* 11, 433. <https://doi.org/10.3390/nano11020433>.
- Bhattacharjee, S., Chaudhary, S.P., and Bhattacharyya, S. (2019). Lead-free metal halide perovskite nanocrystals for photocatalysis in water. Preprint at ChemRxiv. <https://doi.org/10.26434/chemrxiv.9794270.v1>.
- Bresolin, B.-M., Sgarbossa, P., Bahnemann, D.W., and Sillanpää, M. (2020). Cs₃Bi₂I₉/g-C₃N₄ as a new binary photocatalyst for efficient visible-light photocatalytic processes. *Separ. Purif. Technol.* 251, 117320. <https://doi.org/10.1016/j.seppur.2020.117320>.
- Romani, L., Bala, A., Kumar, V., Speltini, A., Milella, A., Fracassi, F., Listorti, A., Profumo, A., and Malavasi, L. (2020). PEA₂SnBr₄: a water-stable lead-free two-dimensional perovskite and demonstration of its use as a co-catalyst in hydrogen photogeneration and organic-dye degradation. *J. Mater. Chem. C* 8, 9189–9194. <https://doi.org/10.1039/D0TC02525A>.
- Romani, L., Speltini, A., Ambrosio, F., Mosconi, E., Profumo, A., Marelli, M., Margadonna, S., Milella, A., Fracassi, F., Listorti, A., et al. (2021). Water-stable DMASnBr₃ lead-free perovskite for effective solar-driven photocatalysis. *Angew. Chem. Int. Ed. Engl.* 60, 3611–3618. <https://doi.org/10.1002/anie.202007584>.
- Dai, Y., and Tüysüz, H. (2019). Lead-free Cs₃Bi₂Br₉ perovskite as photocatalyst for ring-opening reactions of epoxides. *ChemSusChem* 12, 2587–2592. <https://doi.org/10.1002/cssc.201900716>.
- Bresolin, B.-M., Balayeva, N.O., Granone, L.I., Dillert, R., Bahnemann, D.W., and Sillanpää, M. (2020). Anchoring lead-free halide Cs₃Bi₂I₉ perovskite on UV100–TiO₂ for enhanced photocatalytic performance. *Sol. Energy Mater. Sol. Cell.* 204, 110214. <https://doi.org/10.1016/j.solmat.2019.110214>.
- Luo, J., Zhang, W., Yang, H., Fan, Q., Xiong, F., Liu, S., Li, D., and Liu, B. (2021). Halide perovskite composites for photocatalysis: a mini review. *EcoMat* 3. <https://doi.org/10.1002/eom2.12079>.
- Pan, S., Li, J., Wen, Z., Lu, R., Zhang, Q., Jin, H., Zhang, L., Chen, Y., and Wang, S. (2022). Halide perovskite materials for photo(Electro) Chemical applications: dimensionality, heterojunction, and performance. *Adv. Energy Mater.* 12, 2004002. <https://doi.org/10.1002/aenm.202004002>.
- Yuan, J., Liu, H., Wang, S., and Li, X. (2021). How to apply metal halide perovskites to photocatalysis: challenges and development. *Nanoscale* 13, 10281–10304. <https://doi.org/10.1039/D0NR07716J>.
- Han, X., Liu, P., Ran, R., Wang, W., Zhou, W., and Shao, Z. (2022). Non-metal fluorine doping in Ruddlesden–Popper perovskite oxide enables high-efficiency photocatalytic water splitting for hydrogen production. *Mater. Today Energy* 23, 100896. <https://doi.org/10.1016/j.mtener.2021.100896>.
- He, J., Liu, P., Ran, R., Wang, W., Zhou, W., and Shao, Z. (2022). Single-atom catalysts for high-efficiency photocatalytic and photoelectrochemical water splitting: distinctive roles, unique fabrication methods and specific design strategies. *J. Mater. Chem.* 10, 6835–6871. <https://doi.org/10.1039/D2TA00835A>.
- Park, S., Chang, W.J., Lee, C.W., Park, S., Ahn, H.-Y., and Nam, K.T. (2017). Photocatalytic hydrogen generation from hydriodic acid using methylammonium lead iodide in dynamic equilibrium with aqueous solution. *Nat. Energy* 2, 16185. <https://doi.org/10.1038/nenergy.2016.185>.
- Zheng, C., and Rubel, O. (2019). Unraveling the water degradation mechanism of CH₃NH₃PbI₃. *J. Phys. Chem. C* 123, 19385–19394. <https://doi.org/10.1021/acs.jpcc.9b05516>.
- Christians, J.A., Miranda Herrera, P.A., and Kamat, P.V. (2015). Transformation of the excited state and photovoltaic efficiency of CH₃NH₃PbI₃ perovskite upon controlled exposure to humidified air. *J. Am. Chem. Soc.* 137, 1530–1538. <https://doi.org/10.1021/ja511132a>.
- Li, X., Hoffman, J.M., and Kanatzidis, M.G. (2021). The 2D halide perovskite rulebook: how the spacer influences everything from the structure to optoelectronic device efficiency. *Chem. Rev.* 121, 2230–2291. <https://doi.org/10.1021/acs.chemrev.0c01006>.
- Pisanu, A., Speltini, A., Quadrelli, P., Drera, G., Sangaletti, L., and Malavasi, L. (2019). Enhanced air-stability of Sn-based hybrid perovskites induced by dimethylammonium (DMA): synthesis, characterization, aging and hydrogen photogeneration of the MA_{1-x}DMASnBr₃ system. *J. Mater. Chem. C* 7, 7020–7026. <https://doi.org/10.1039/C9TC01743G>.
- Ju, D., Zheng, X., Liu, J., Chen, Y., Zhang, J., Cao, B., Xiao, H., Mohammed, O.F., Bakr, O.M., and Tao, X. (2018). Reversible band gap narrowing of Sn-based hybrid perovskite single crystal with excellent phase stability. *Angew. Chem. Int. Ed. Engl.* 57, 14868–14872. <https://doi.org/10.1002/anie.201810481>.
- Hong, Z., Chong, W.K., Ng, A.Y.R., Li, M., Ganguly, R., Sum, T.C., and Soo, H.S. (2019). Hydrophobic metal halide perovskites for visible-light photoredox C–C bond cleavage and dehydrogenation catalysis. *Angew. Chem. Int. Ed. Engl.* 58, 3456–3460. <https://doi.org/10.1002/anie.201812225>.
- Chiara, R., Morana, M., Boiocchi, M., Coduri, M., Striccoli, M., Fracassi, F., Listorti, A., Mahata, A., Quadrelli, P., Gaboardi, M., et al. (2021). Role of spacer cations and structural distortion in two-dimensional germanium halide perovskites. *J. Mater. Chem. C* 9, 9899–9906. <https://doi.org/10.1039/D1TC02394B>.
- Venkatesan, N.R., Mahdi, A., Barraza, B., Wu, G., Chabiny, M.L., and Seshadri, R. (2019). Enhanced yield-mobility products in hybrid halide Ruddlesden–Popper compounds with aromatic ammonium spacers. *Dalton Trans.* 48,

- 14019–14026. <https://doi.org/10.1039/C9DT03074C>.
26. Malavasi, L., Morana, M., and Chiara, R. (2021). Germanium-based halide perovskites: materials, properties, and applications. *ChemPlusChem* 86, 879–888. <https://doi.org/10.1002/cplu.202100191>.
 27. Chen, M., Ju, M.-G., Garcés, H.F., Carl, A.D., Ono, L.K., Hawash, Z., Zhang, Y., Shen, T., Qi, Y., Grimm, R.L., et al. (2019). Highly stable and efficient all-inorganic lead-free perovskite solar cells with native-oxide passivation. *Nat. Commun.* 10, 16. <https://doi.org/10.1038/s41467-018-07951-y>.
 28. Prabhakaran, K., and Ogino, T. (1995). Oxidation of Ge(100) and Ge(111) surfaces: an UPS and XPS study. *Surf. Sci.* 325, 263–271. [https://doi.org/10.1016/0039-6028\(94\)00746-2](https://doi.org/10.1016/0039-6028(94)00746-2).
 29. Wagner, C.D., Zatko, D.A., and Raymond, R.H. (1980). Use of the oxygen KLL Auger lines in identification of surface chemical states by electron spectroscopy for chemical analysis. *Anal. Chem.* 52, 1445–1451. <https://doi.org/10.1021/ac50059a017>.
 30. Meggiolaro, D., Ricciarelli, D., Alasmari, A.A., Alasmay, F.A.S., and De Angelis, F. (2020). Tin versus lead redox chemistry modulates charge trapping and self-doping in tin/lead iodide perovskites. *J. Phys. Chem. Lett.* 11, 3546–3556. <https://doi.org/10.1021/acs.jpcllett.0c00725>.
 31. Ricciarelli, D., Kaiser, W., Mosconi, E., Wiktor, J., Ashraf, M.W., Malavasi, L., Ambrosio, F., and De Angelis, F. (2022). Reaction mechanism of photocatalytic hydrogen production at water/tin halide perovskite interfaces. *ACS Energy Lett.* 7, 1308–1315. <https://doi.org/10.1021/acsenergylett.2c00122>.
 32. Sharma, A., Varshney, M., Chae, K.H., and Won, S.O. (2018). Mechanistic investigations on emission characteristics from g-C3N4, g-C3N4@Pt and g-C3N4@Ag nanostructures using X-ray absorption spectroscopy. *Curr. Appl. Phys.* 18, 1458–1464. <https://doi.org/10.1016/j.cap.2018.08.019>.
 33. Yuan, Y., Zhang, L., Xing, J., Utama, M.I.B., Lu, X., Du, K., Li, Y., Hu, X., Wang, S., Genç, A., et al. (2015). High-yield synthesis and optical properties of g-C3N4. *Nanoscale* 7, 12343–12350. <https://doi.org/10.1039/C5NR02905H>.
 34. Romani, L., Speltini, A., Dibenedetto, C.N., Listorti, A., Ambrosio, F., Mosconi, E., Simbula, A., Saba, M., Profumo, A., Quadrelli, P., et al. (2021). Experimental strategy and mechanistic view to boost the photocatalytic activity of Cs₃Bi₂Br₉ lead-free perovskite derivative by g-C₃N₄ composite engineering. *Adv. Funct. Mater.* 31, 2104428. <https://doi.org/10.1002/adfm.202104428>.
 35. Cao, S., Low, J., Yu, J., and Jaroniec, M. (2015). Polymeric photocatalysts based on graphitic carbon nitride. *Adv. Mater.* 27, 2150–2176. <https://doi.org/10.1002/adma.201500033>.
 36. Speltini, A., Romani, L., Dondi, D., Malavasi, L., and Profumo, A. (2020). Carbon nitride-perovskite composites: evaluation and optimization of photocatalytic hydrogen evolution in Saccharides aqueous solution. *Catalysts* 10, 1259. <https://doi.org/10.3390/catal10111259>.
 37. Kaiser, W., Ricciarelli, D., Mosconi, E., Allothman, A.A., Ambrosio, F., and De Angelis, F. (2022). Stability of tin- versus lead-halide perovskites: Ab initio molecular dynamics simulations of perovskite/water interfaces. *J. Phys. Chem. Lett.* 13, 2321–2329. <https://doi.org/10.1021/acs.jpcllett.2c00273>.